Time-average measurement of velocity, density, temperature, and turbulence using molecular Rayleigh scattering

by

A.F. Mielke[(1)*], R.G. Seasholtz[(1)], K.A. Elam[(2)], and J. Panda[(3)]

[(1)]NASA Glenn Research Center, Cleveland, Ohio 44135, USA
[(2)]Akima Corporation, Fairview Park, Ohio 44126, USA
[(3)]OAI, Brook Park, Ohio 44142, USA
[*]E-Mail: Amy.F.Mielke@nasa.gov

ABSTRACT

Measurement of time-averaged velocity, density, temperature, and turbulence in gas flows using a nonintrusive, point-wise measurement technique based on molecular Rayleigh scattering is discussed. Subsonic and supersonic flows in a 25.4-mm diameter free jet facility were studied. The developed instrumentation utilizes a Fabry-Perot interferometer to spectrally resolve molecularly scattered light from a laser beam passed through a gas flow. The spectrum of the scattered light contains information about velocity, density, and temperature of the gas. The technique uses a slow scan, low noise 16-bit depth CCD camera to record images of the fringes formed by Rayleigh scattered light passing through the interferometer. A kinetic theory model of the Rayleigh scattered light is used in a nonlinear least squares fitting routine to estimate the unknown parameters from the fringe images. The ability to extract turbulence information from the fringe image data proved to be a challenge since the fringe is broadened by not only turbulence, but also thermal fluctuations and aperture effects from collecting light over a range of scattering angles. Figure 1 illustrates broadening of a Rayleigh spectrum typical of flow conditions observed in this work due to aperture effects and turbulence for a scattering angle, c_s, of 90°, *f*/3.67 collection optics, mean flow velocity, u_k, of 300 m/s, and turbulent velocity fluctuations, s_{uk}, of 55 m/s. The greatest difficulty in processing the image data was decoupling the thermal and turbulence broadening in the spectrum. To aid in this endeavor, it was necessary to seed the ambient air with smoke and dust particulates; taking advantage of the turbulence broadening in the Mie scattering component of the spectrum of the collected light (not shown in the figure). The primary jet flow was not seeded due to the difficulty of the task. For measurement points lacking particles, velocity, density, and temperature information could reliably be recovered, however the turbulence estimates contained significant uncertainty. Resulting flow parameter estimates are presented for surveys of Mach 0.6, 0.95, and 1.4 jet flows. Velocity, density, and temperature were determined with accuracies of 5 m/s, 1.5%, and 1%, respectively, in flows with no particles present, and with accuracies of 5 m/s, 1-4%, and 2% in flows with particles. Comparison with hotwire data for the Mach 0.6 condition demonstrated turbulence estimates with accuracies of about 5 m/s outside the jet core where Mie scattering from dust/smoke particulates aided in the estimation of turbulence. Turbulence estimates could not be recovered with any significant accuracy for measurement points where no particles were present.

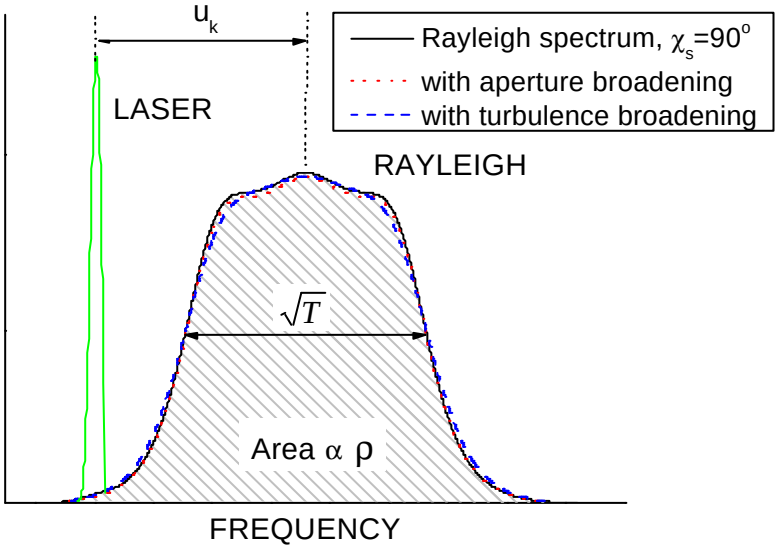

Fig. 1. Rayleigh scattering spectra for Mach 0.95 flow, s_{uk} = 55 m/s, f/3.67 collection optics, c_s = 90°.

1. INTRODUCTION

A molecular Rayeigh scattering technique has been developed to measure velocity, density, temperature, and turbulence in sparsely seeded gas flows, and was used to make measurements in a 25.4-mm diameter free jet facility which operates at subsonic and supersonic flow conditions. This measurement technique is useful for obtaining critical information for validation of computational fluid dynamics (CFD) codes. The non-intrusive technique is attractive to researchers studying supersonic flows where the environment is too harsh for intrusive instruments like hotwires, which disturb the flow and can only be applied to low temperature subsonic flows.

Point-wise measurements of turbulence intensity are traditionally obtained using hot wire anemometry or Laser-Doppler Velocimetry (LDV) (Lau, et al. 1979, 1981, Flack 1982, and Heist and Castro 1996). However, these techniques have obvious disadvantages. Hot wire anemometry requires that a physical probe be placed in the flow field, hence disturbing the true flow characteristics. Although LDV is a nonintrusive technique, it requires seeding of the flow and is not capable of providing simultaneous temperature and density measurements. Other optical based techniques for measuring turbulence intensity exist. Elliot and Boguszki (2001) investigated a filtered Rayleigh scattering technique to make turbulence intensity measurements using a pulsed laser to get instantaneous quantities. Transient gradient spectroscopy (TGS) (Li, et al. 2002), also known as Laser-Induced Thermal Acoustics (LITA) (Hart, et al. 1999), is a point-wise technique that measures instantaneous temperature, velocity, and species concentrations, and is capable of providing turbulence information. Bridges, et al. (2003) used Particle Image Velocimetry (PIV) to calculate turbulence in nozzle flows from instantaneous 2-D velocity maps. Garg and Settles (1998) developed a technique based on focusing schlieren deflectometry to make turbulence measurements in compressible flows. The Rayleigh scattering technique presented is unique in that it provides simultaneous time-average velocity, density, temperature, and turbulence measurements at a point in a flow field. The ability to obtain multiple property measurements simultaneously is a valuable tool for jet flow research.

Molecular Rayleigh scattering is the result of elastic light scattering from gas molecules. When light from a single frequency laser beam passes through a gas, the scattered light is shifted in frequency by the Doppler effect due to the bulk motion of the molecules. The optical frequency spectrum contains information about the gas density, bulk velocity, and temperature. Figure 1 shows a Rayleigh scattering spectrum containing the narrow laser line and the Rayleigh spectral peak for 90^o-degree scattering, which was the scattering angle used in this work. The shape of the spectrum is dependent on gas density and scattering angle. For low velocity, low density flows observed with 90^o-scattering, the spectrum is accurately modeled by a Gaussian function. As the gas density increases, the spectrum deviates from a Gaussian as shown by the Rayleigh spectrum (solid line) in figure 1. If the gas composition is known, the total intensity of the Rayleigh scattered light is directly proportional to the gas density. The frequency shift between the laser peak and the Rayleigh peak is proportional to the bulk flow velocity. The width of the spectrum is related to the gas temperature. As shown in the figure, other factors may alter the shape of the spectrum. Turbulent velocity fluctuations broaden the spectrum and wash out the spectral shape features that may be present. The spectral broadening related to the range of scattering angles across the collection lens aperture appears to be negligible for 90^o-scattering with f/3.67 collection optics, as in this experiment. As scattering angle decreases (towards forward-scattering) the spectrum develops side lobes known as Brillioun peaks as shown in figure 2. This figure illustrates spectral broadening due to turbulence and aperture effects for the flow observed with 25^o-scattering.

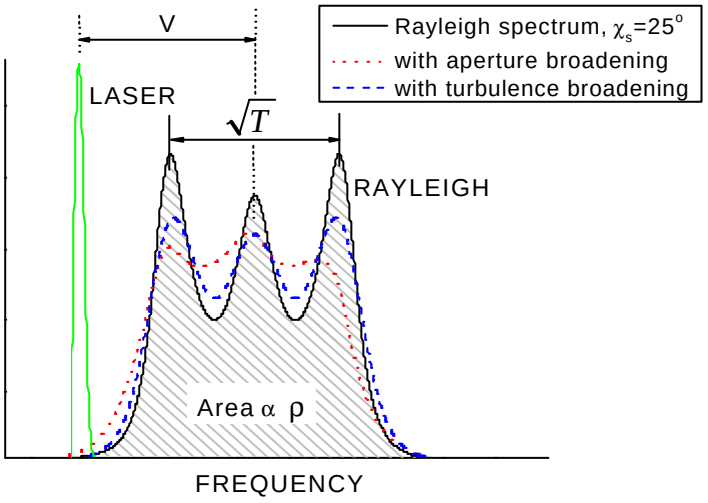

Fig. 2. Rayleigh scattering spectra for Mach 0.95 flow, s_{uk} = 55 m/s, f/3.67 collection optics, $c_s = 25^o$

At near-forward-scattering ($c_s < 90^o$), the shape of the spectrum changes very rapidly with scattering angle; in this situation it is important to consider aperture broadening. The aperture broadened spectrum is actually asymmetric under these conditions. The aperture broadening for near-forward scattering angles is significant and must be included in the model function for spectral analysis at such scattering angles. Only 90^o-scattering was used in this work, but we may modify our experimental arrangement to collect light at other scattering angles in future work. The additional structure of the spectrum should enhance the ability to recover turbulence information from the Rayleigh scattering light.

A Fabry-Perot interferometer operated in the static imaging mode is used to analyze the scattered light, and a low noise CCD camera is used to record the circular interference fringe pattern containing the spectral information. Nonlinear least squares analysis based on a kinetic theory model of the Rayleigh scattering process provides estimates of velocity, density, temperature, and turbulence for each data point. Previous work by Seasholtz and Greer (1998) and Panda and Seasholtz (1999) used a similar technique to measure velocity and temperature in harsh environments. Mielke, et al. (2004) further developed this technique and demonstrated velocity, density, and temperature measurements in the jet facility used in the current work. Turbulence information could not be extracted previously due to either low turbulence levels causing little broadening of the spectrum, or low velocities where the shape of the spectrum is nearly Gaussian. In both cases it was impossible to differentiate the turbulence broadening from the thermal broadening in the Rayleigh spectrum. To overcome these difficulties in the current work, particles were added to flow regions around the primary jet so that broadening of the particle, or Mie, scattering spectrum could be used as an independent measure of the turbulent velocity fluctuations. The Mie scattering spectrum has a narrow linewidth peak shifted in frequency from the incident laser light by the Doppler effect due to the bulk motion of the particles. Due to inherent difficulties, particles were not added within the jet core for these measurements. It will be shown that this technique can provide velocity, density, and temperature measurements with and without particles in the flow; however particle scattering is necessary in experimental arrangements with 90^o-scattering in order to obtain turbulence measurements.

2. THEORY

An appropriate model function of the interference pattern containing the spectral information of the scattered light is needed for least squares fitting of the fringe image data. The model must include the Rayleigh and Mie scattering components and modeling of the turbulence. Various models are available for the Rayleigh component of the spectrum. The validity of each model depends on the density of the gas, which greatly affects the shape of the spectrum. A non-dimensional parameter y is used to define density regimes:

$$y = \frac{p}{h\mathrm{K}a} \tag{1}$$

where p is the gas pressure, h is the gas viscosity, K is the magnitude of the interaction wave vector $\mathbf{K}$ that defines the direction of the velocity component, u_k, being measured, and a is the most probable molecular speed defined as

$$a = \sqrt{\frac{2kT}{m}} \tag{2}$$

where k is the Boltzmann constant, T is the fluid temperature, and m is the molecular mass. The interaction wave vector is the bisection of the incident and scattered light wave vectors. The magnitude of the interaction wave vector is:

$$\mathrm{K} = |\mathbf{K}| = \frac{4p}{l}\left[\sin\frac{c_s}{2}\right] \tag{3}$$

where l is the wavelength of the incident light and c_s is the scattering angle between the incident and scattered light wave vectors. The geometry of the optical arrangement in an experiment can be designed such that the desired velocity component is measured.

Three density regimes are defined for typical 90^o-scattering (Greytak and Benedek 1966). For low density gases where $y<<1$, the Rayleigh spectrum is accurately modeled by a Gaussian function. For higher density gases where $y>>1$, the Gaussian model is not accurate since the Rayleigh spectrum broadens and eventually develops side-lobes known as Brillouin peaks. In this regime, a Continuum model is valid. Finally, when $y \sim 1$, as is the case in these experiments, a kinetic theory model is required. A model developed by G. Tenti (Boley, et al. 1972, Tenti, et al. 1974) provides a kinetic model of Rayleigh-Brillouin scattering from molecular gases in all density regimes. The TENTI S6 model is the chosen spectrum model for least-squares fitting of our data. The spectra shown in figures 1 and 2 illustrate the kinetic and continuum regimes, respectively, and were simulated using the TENTI S6 model.

The spectrum of the Rayleigh scattered light is analyzed using a planar mirror Fabry-Perot interferometer operated in the static imaging mode (Vaughan 1989). The fringes at the output of the interferometer are focused onto a CCD detector. The fringe intensity pattern is a function of the Rayleigh spectrum, S_R, and the Fabry-Perot instrument function, I_{FP}. The Fabry-Perot instrument function is:

$$I_{FP}(x_f, r) = \frac{1}{1 + F\sin^2\dfrac{y(x_f, r)}{2}} \tag{4}$$

where $F = \dfrac{1}{\sin^2\left(\dfrac{p}{2N_e}\right)}$, (5)

ψ is the phase change of the light between successive reflections given by:

$$y = \frac{4p\ m\ d}{l}\left[\frac{q_R^2 - q^2}{2} + \frac{la}{c\Lambda}x_f\right], \tag{6}$$

N_e is the effective finesse, m is the refractive index of the medium in the Fabry-Perot cavity, d is the Fabry-Perot mirror spacing, q is the angle between the ray and optical axis ($q_R = r_R/f_L$, $q = r/f_L$), r_R is the fringe radius of the reference laser light, r is the radial position in the image plane, f_L is the fringe forming lens focal length, $\Lambda = 2\pi/K$, and x_f is the dimensionless frequency defined as

$$x_f = \frac{2p(f - f_0)}{Ka}, \tag{7}$$

where f-f_0 is the frequency shift between the reference laser light and the Rayleigh scattered light.

In our experiment, Rayleigh scattered light from a defined probe volume is collected into a multimode optical fiber. The fiber carries the light to another area where a Fabry-Perot interferometer is used to spectrally resolve the light. A low-noise CCD camera is placed at the output of the Fabry-Perot interferometer and a fringe forming lens focuses the interference fringe pattern onto the CCD detector. The total expected number of photoelectron counts incident on the detector plane without the Fabry-Perot interferometer in the optical path is expressed as:

$$\langle N_R \rangle = \frac{e\ P_0\ n\ L_x\ l\ \Omega\ \Delta t}{h\,c}\left(\frac{ds}{d\Omega}\right)sin^2\ c_s \tag{8}$$

where ε is the overall system efficiency including detector quantum efficiency and other losses, P_0 is the power of the incident laser beam, n is the molecular number density, L_x is the probe volume length, Ω is the solid light collection angle, Δt is the data acquisition time, $\left(\frac{ds}{d\Omega}\right)$ is the differential scattering cross-section of the gas molecules, h is Planck's constant, and c is the speed of light. If we assume that the illumination is uniform over the entire fiber face, then the model function for the amount of energy collected on the q^{th} pixel of the detector, expressed as photoelectron counts including light at the laser frequency, light scattered from particles (Mie scattering) and background light, as imaged through the Fabry-Perot, is:

$$\langle N_q \rangle = \frac{\langle N_R \rangle}{p\ r_{max}^2}\int_{y_q}^{y_q+e_p}\int_{x_q}^{x_q+e_p}\int_{-\infty}^{+\infty} S_R(x_f)I_{FP}(x_f, r)dx_f\,dxdy + \frac{A_f}{e_p^2}\int_{y_q}^{y_q+e_p}\int_{x_q}^{x_q+e_p} I_{FP}(x_{f_0}, r)dxdy$$

$$+ \frac{A_p}{e_p^2}\int_{y_q}^{y_q+e_p}\int_{x_q}^{x_q+e_p} I_{FP}(x_f, r)dxdy + B_g \tag{9}$$

where r_{max} is the radius of the image of the fiber face, (x,y) are the position coordinates in the image plane, $r = \sqrt{(x-x_0)^2 + (y-y_0)^2}$ where (x_0,y_0) are the coordinates of the center of the fringe pattern, (x_q,y_q) are the coordinates of the lower left corner of the q^{th} pixel, e_p is the pixel width (square pixels are assumed), A_f is the amplitude of light at the laser frequency, A_p is the amplitude of the light scattered from particles, and B_g is the amount of broadband light. The parameters A_f, A_p, and B_g are relative photoelectron counts in terms of CCD grey levels. If the flow is turbulent, the Rayleigh scattering spectrum S_R in equation (9) is replaced by the following spectrum:

$$S_T(x_f, \overline{u_k}, s_{u_k}) = \int_{-\infty}^{\infty} S_R(x_f, u_k)\,p(u_k, \overline{u_k}, s_{u_k})du_k \tag{10}$$

and the model of the particle scattering is modified as:

$$\frac{A_p}{e_p^2}\int_{y_q}^{y_q+e_p}\int_{x_q}^{x_q+e_p}\int_{-\infty}^{\infty} p(u_k, \overline{u_k}, s_{u_k})I_{FP}(x_f, r)du_k\,dxdy \tag{11}$$

where a Gaussian probability distribution is assumed for the velocity component, u_k,

$$p(u_k, \overline{u_k}, s_{u_k}) = \frac{1}{(2p)^{1/2}s_{u_k}}e^{-\frac{1}{2}\left(\frac{u_k - \overline{u_k}}{s_{u_k}}\right)^2} \tag{12}$$

and the turbulent fluctuations are assumed to be isotropic with standard deviation:

$$s_{u_k} = \left[\left(u_k - \overline{u_k}\right)^2\right]^{1/2} \tag{13}$$

This model function is used to estimate the unknown parameters from the experimental data.

2.1 Measurement uncertainty

The lower bound on the uncertainty in velocity, density, temperature, and turbulence measurements using Rayleigh scattering is set by the photon statistical noise. Estimates of the measurement uncertainty in the unknown parameters for this technique were obtained by calculating the Cramer-Rao lower bound (Whalen 1971). For a measurement that is a function of a set of unknown parameters, $\hat{a}_i$, the variance of the estimates of the parameters is:

$$V(\hat{a}_i) = \left[\Gamma^{-1}\right] \tag{14}$$

where G is the Fisher information matrix, which for Poisson statistics is given by:

$$\Gamma_{i,j} = \sum_q \frac{1}{\langle N_q \rangle} \frac{\partial \langle N_q \rangle}{\partial a_i} \frac{\partial \langle N_q \rangle}{\partial a_j} \tag{15}$$

A process governed by Poisson statistics is one in which the mean is equal to the variance. In this case, the mean of the photon counts is theoretically equal to the variance of the counts.

The Cramer-Rao lower bound estimates for our actual Fabry-Perot interferometer and CCD system assuming the TENTI S6 spectral model for the Rayleigh scattered light and including CCD read noise, overall optical efficiency of the system, and other significant factors, have been calculated for various flow situations. In previous work (Mielke, et al. 2004) the lower bound uncertainty in velocity, density, and temperature measurements when fitting for velocity, u_k, density, r, temperature, T, turbulence, s_{uk}, and fringe center position, (x_0, y_0) with negligible particle scattering were calculated as 0.3 m/s, 0.1%, and 0.3%, respectively. In the same work it was shown that the lower bound measurement uncertainty in s_{uk} decreased as y-parameter increased since the shape of the spectrum deviates from a Gaussian as y increases. It was also observed that the uncertainty in s_{uk} decreased as s_{uk} increased.

Recovery of turbulence information improves when particles are added to the flow. The lower bound measurement uncertainty in velocity, density, temperature, and turbulence were calculated over a range of particle scattering amplitudes, A_p, from 0 to 3000 grey levels. Figure 3 gives the uncertainty in s_{uk} as a function of A_p and s_{uk} for Mach 0.6 flow conditions. In this flow, typical s_{uk} values range from ~3-35 m/s, depending on location within the flow field. The uncertainty in s_{uk} significantly decreases with the introduction of particles in the flow. Similarly, uncertainty in velocity also decreases as A_p increases since the frequency shift of the particle scattering peak gives an additional measurement of velocity. The uncertainty in s_{uk} is lower for higher turbulence levels. Minimum uncertainty in density and temperature measurements occurs for $A_p \sim 250$ grey levels as shown in figure 4. Although increased particle scattering improves the velocity and turbulence measurements, there is potential for degradation of the density and temperature measurements if the particle scattering becomes too great. Unfortunately the turbulence measurement uncertainty is quite large at the particle scattering level that is optimum for density and temperature measurements. A_p should be greater than about 1500 grey levels in order to recover accurate turbulence estimates in this experiment. The Rayleigh fringe generally had amplitude of about 1600 grey levels, so the particle scattering intensity level should be greater than or equal to the Rayleigh scattering level. The lower bound uncertainties in velocity, density, temperature, and turbulence for particle scattering amplitude, A_p, of 1500 grey levels are 0.07 m/s, 0.1%, 0.2%, and 0.5-2 m/s, respectively.

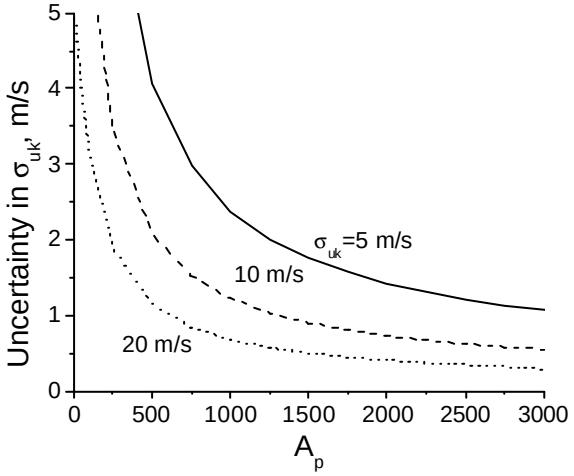

Fig. 3. Uncertainty in s_{uk} as a function of particle scattering amplitude for s_{uk} values of 5, 10, and 20 m/s.

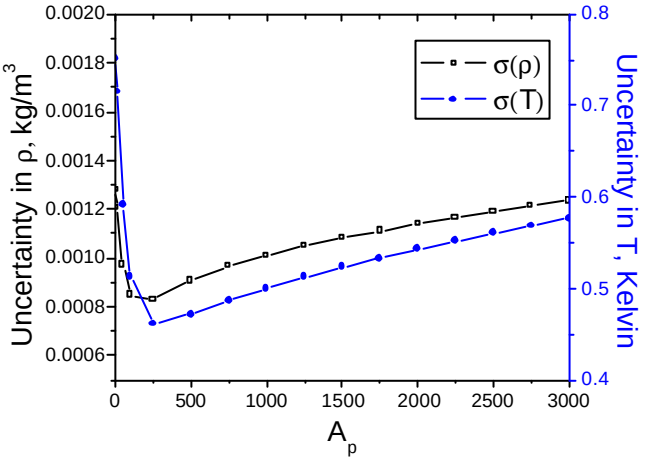

Fig. 4. Uncertainty in density and temperature as a function of particle scattering amplitude for s_{uk} = 5m/s.

In previous work (Mielke, et al. 2004), simulated images of fringe patterns using the developed model function were generated for Mach 0.6 flow conditions with varying levels of turbulence, and then processed with the least-squares fitting routine assuming no turbulence. This exercise demonstrated that temperature estimates were not significantly affected (errors < 2%) if turbulence was neglected in the model when turbulence levels were less than 80m/s. Therefore, we can still obtain reliable velocity, density, and temperature information by neglecting the turbulence broadening in the Rayleigh spectrum when turbulence cannot be extracted due to the limitations discussed above.

In summary, the uncertainty analysis shows that the ability to extract turbulence information from the spectrum improves as the Rayleigh spectrum deviates from a Gaussian (y > 0.8) and with the introduction of particles in the flow. Also, the accuracy of the density and temperature measurements may be sacrificed if particle scattering levels are too high. Particle scattering amplitude should be similar in magnitude to the Rayleigh scattering amplitude (~1500 grey levels) to provide accurate turbulence measurements and not degrade the density and temperature measurements. In situations where

turbulence cannot be extracted from the spectral analysis, it is reasonable to assume turbulence is negligible in order to obtain accurate velocity, density, and temperature measurements as long as the turbulence intensity is less than 80m/s.

3. EXPERIMENT

Flow measurements were made in a 25.4-mm diameter free jet facility at the NASA Glenn Research Center using the described Rayleigh scattering measurement technique. A convergent nozzle provided subsonic flow conditions and a convergent-divergent nozzle designed by the method of characteristics provided Mach 1.4 flow. The experiment was set up in two parts. The first part consisted of the laser and collection optics constructed around the jet facility to collect Rayleigh scattered light from gas molecules in the jet flow and Mie scattered light from particles in the flow. This light was collected into an optical fiber and routed to another room where the spectral analysis took place. The second part of the setup included the equipment for spectral analysis, consisting of a Fabry-Perot interferometer and CCD camera. This equipment was very sensitive to vibrations and temperature fluctuations; hence it was kept in a separate room to isolate it from the noise and accompanying vibrations associated with the high speed jet. The upper part of figure 5 shows the experimental arrangement around the jet facility, while the lower part shows the arrangement of the sensitive optical analysis equipment.

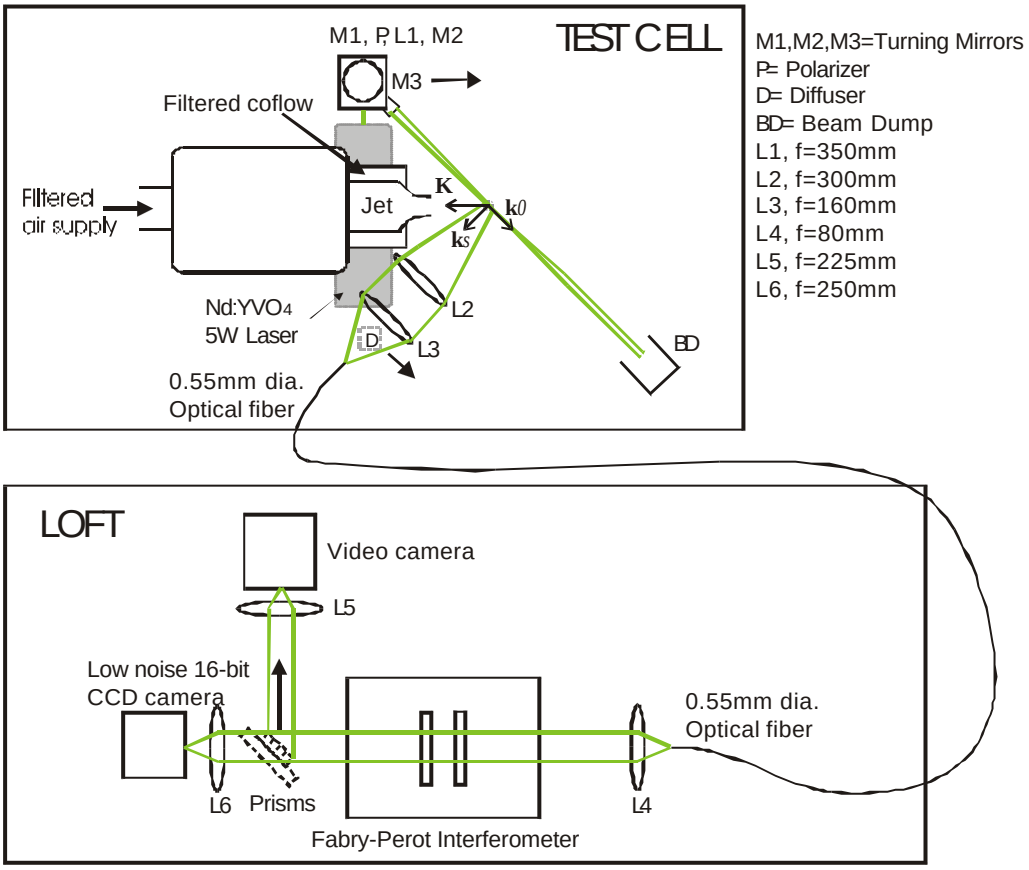

Fig. 5. Schematic of the experimental arrangement.

In past experiments (Mielke, et al. 2004) extensive measures were taken to eliminate particles and condensation from the flow so that only Rayleigh scattered light was collected. For example, a filtered co-flow was used around the jet to eliminate particles from being entrained into the flow. In the current work, particles were desired in the flow since the additional information contained in the Mie scattering from particles was utilized to obtain turbulence information. Therefore, the co-flow was not used in the experiments discussed here. The amount of particle seeding required towards this goal was very small. In fact, the dust in the room air usually provided sufficient seeding. In some cases incense was burned in the test cell to provide additional scatterers. The particle number density and size distribution were unknown, although they were assumed to be very small and follow the flow accurately. The air supplied to the jet was filtered and dried prior to arriving at the facility. Therefore, flow in the jet core contains few or no particles. Under these conditions it may be difficult to recover turbulence information in the jet core. The jet core flow was not seeded due to the difficulties involved and the fact that an advantage of Rayleigh scattering is usually that flow seeding is unnecessary. Therefore, the core flow was not seeded so as to determine the ability of the technique to extract turbulence when particles were not present.

A 5-Watt 532-nm Nd:Vanadate CW laser with a 2.25-mm output beam diameter provided the incident light for the system. The laser was located in the test cell near the jet and was kept in an anechoic box to eliminate modulation of the laser frequency imposed by jet noise. The beam was focused by a 350-mm focal length lens to a 200-µm diameter beam at the probe volume. Rayleigh scattering is polarization dependent, so a half-wave plate was used to align the peak scattering plane

with the collection optics. As shown in figure 5, the beam is aligned at a 45^o angle to the jet axis and parallel to the ground. Scattered light was collected at a nominal angle of 90^o to the incident light propagation direction. The vector diagram in figure 5 illustrates how the incident and scattered light wave vectors were arranged to result in measurement of the axial component of the velocity. The light was first collimated by an f/3.67 300-mm focal length achromat and then focused by a 160-mm focal length achromat onto the face of a 550-µm diameter multimode optical fiber. This optical arrangement provided a probe volume with a length of 1.03-mm and height of 200-µm. The laser, transmitting optics, and receiving optics were all mounted on the same axial-radial traversing mechanism so that the probe volume could be positioned anywhere in the flow field without requiring realignment of the optics.

A 20-m length optical fiber carried the scattered light to the room where the interferometer and detection optics were located. The light exiting the fiber was collimated by an 80-mm focal length lens and directed through the planar mirror Fabry-Perot interferometer. The interferometer had 70-mm diameter mirrors with 85% reflectivity, 9.6 GHz free spectral range (FSR), and reflective finesse of approximately 19. The Fabry-Perot interferometer operated in the static imaging mode consists of an etalon, or two perfectly parallel mirrors, and the distance between the mirrors determines the interference fringe radius. The Fabry-Perot is an extremely sensitive instrument; even the smallest vibrations or temperature changes can cause the mirrors to drift out of parallel alignment. If this happens, the spectral measurements will have increased uncertainty. Therefore, a stabilization routine was utilized to maintain alignment of the mirrors during testing. Towards this goal, a mirror and diffuser shown in the schematic of the setup around the jet were placed in the beam path by linear actuators while Rayleigh scattering measurements were not being performed to direct light from the incident laser beam into the fiber and through the interferometer. A set of prisms mounted on another linear actuator at the output of the interferometer were placed in the optical path to direct light from three regions on the interferometer mirrors to a video camera. The live video of the three fringe images was used in a feedback control loop to adjust the mirror positions using piezoelectric transducers until the three fringes were equal in diameter. This system was also used to set the fringe diameter of the incident reference light. For more details on the stabilization system for the Fabry-Perot interferometer refer to Seasholtz, et al. (2002).

When collecting data the prisms were moved out of the optical path and the light exiting the Fabry-Perot was focused by a 250-mm focal length fringe forming lens onto the detector of a slow scan, low noise, cooled CCD camera with 27-µm square pixels and 16-bit depth per pixel. This formed a 1.72-mm (64 pixel) diameter image of the fiber face at the detector plane. The diameter of the optical fiber limited us to imaging only the central fringe of the concentric fringe interference pattern.

The following procedure was followed when acquiring data in the jet facility. With mirror, diffuser, and prisms in the optical path, the stabilization routine was used to align the mirrors of the interferometer and to set the reference fringe radius at the desired target value. For this work, a reference fringe radius of about 23 CCD pixels was used. At each data point, the stabilization was paused while the prisms were removed from the optical path. The fringe pattern formed from incident laser light passing through the interferometer was recorded by the CCD camera using a 10 ms exposure time. Figure 6(a) shows a typical reference fringe image from the experiments. Next, the mirror and diffuser were removed from the beam path so that light scattered from the probe volume was collected into the fiber. Two consecutive images of the fringe pattern associated with the Rayleigh scattered light were recorded by the CCD camera using an exposure time of 1 s. Figure 6(b) shows a typical fringe image formed by Rayleigh scattered light. The region of the detector where the measurements were taken had some bad pixels in the lower right quadrant. These pixels were not used in the image processing. The Rayleigh fringe shown corresponds to a velocity of 150 m/s. The peak of the Rayleigh fringe is shifted from the reference fringe by the Doppler shift associated with this velocity. For our experimental arrangement, the fringe diameter decreased as velocity increased. The Rayleigh fringe is more diffuse than the reference fringe due to thermal broadening. The narrow peak superimposed on the Rayleigh peak is due to scattering from particles. This peak is also shifted from the reference laser peak by the Doppler shift. Both the Rayleigh spectral peak and the Mie spectral peak are broadened by turbulent velocity fluctuations.

After the two Rayleigh fringe images were recorded, the mirror and diffuser were replaced in the beam path and a second reference laser fringe image was recorded. A reference fringe image was recorded before and after the Rayleigh data acquisition because the laser frequency had a tendency to drift over time and the second reference image was used as a check to reject data in which the laser frequency drifted by a significant amount. Finally, the prisms were moved back into the optical path and control was restored to the Fabry-Perot stabilization routine to reestablish the desired fringe radius, in case the system had drifted during data acquisition. This procedure was repeated for each measurement point.

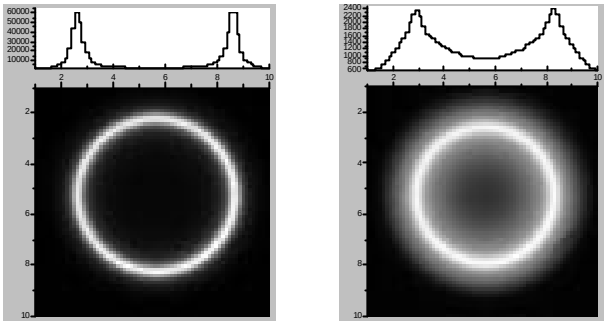

(a) (b)

Fig. 6. (a) Reference laser fringe; (b) Rayleigh scattering fringe containing particle Scattering: velocity = 150m/s, temperature =283 K,and density =1.21 kg/m^3.

4. RESULTS AND DISCUSSION

4.1 Calibration

To determine various parameters defined by the optical system, a series of reference fringe images were acquired over a range of radii from 200 – 750 μm. These images were fit for amplitude of the reference laser fringe, A_f, effective finesse, N_e, fringe radius, r_R, and fringe center position, (x_0,y_0). The baseline noise level was accounted for by subtracting a mean value at each pixel obtained from a series of images taken with the camera shutter closed. We observed that the fringe amplitude and effective finesse were not constant over the image plane. The nonuniformity of these parameters may have been due to defocusing with increasing radial distance from the lens centerline, or imperfections in the Fabry-Perot mirrors. Profiles of finesse and intensity with radial distance in the image plane were determined from the reference fringe images. Second order polynomial fits with the square of the radius were used for both the finesse and intensity profiles. The intensity profile was used in all subsequent image processing, and the finesse profile was used as a starting point for obtaining the finesse profile that yielded the best results in all flow conditions.

Fitting for particle scattering using the developed model function was very sensitive to finesse value. Therefore, image data containing particle scattering was used to fine-tune the radial finesse profile. Isentropic flow equations cannot be used for flow calculations outside of the potential core where particles were present. Instead, hotwire measurements taken at several radial locations at an axial position 6 diameters downstream of the nozzle exit were used as known velocity, u_k, and turbulence, s_{uk}, values for Rayleigh data taken at the same locations. The Crocco-Busemann (C-B) relations (White, 1973) were used to estimate density, r, and temperature, T, from the hotwire velocity measurements. These known values were used in the model while fitting for overall efficiency factor, ε, center position (x_0,y_0), reference fringe radius, r_R, particle scattering amplitude, A_p, scattering angle, χ_s, and coefficients for the finesse profile, $B1_{Ne}$, $B2_{Ne}$, A_{Ne} (where $N_e = A_{Ne} + B1_{Ne}\, r^2 + B2_{Ne}\, r^4$, r in μm). The reference radius fit in the Rayleigh image data tended to differ by a nearly constant amount from the value obtained from the corresponding reference fringe image. Therefore, a constant offset determined from this calibration was applied to r_R values obtained from the reference images when fitting for the flow parameters. The mean values of ε, c_s, $B1_{Ne}$, $B2_{Ne}$, and A_{Ne} were calibrated and used in the model function when fitting for flow parameters with particles present. Nominal values were: ε = 0.8%, c_s = 91.2°, r_R-shift = 6 μm, $B1_{Ne}$ = 7.27e-6, $B2_{Ne}$ = -1.1e-11, and A_{Ne} = 17.2.

While performing the image processing, it became apparent that the model struggled to fit the density and temperature values properly when turbulence was included in the Rayleigh spectrum model, even when particles were present in the probe volume. Since the uncertainty analysis showed that the temperature estimates are not compromised by artificially assuming no turbulence, turbulence was neglected in the Rayleigh spectrum model. Therefore, the turbulence estimates were solely computed frombroadening of the particle scattering spectrum.

Fringe images for Rayleigh scattered light were acquired in the potential core of subsonic flows over a range of velocities from 25 to 300 m/s (y = 0.8-1.0) to validate the measurement technique. The fitting routine behaved differently when particles were not present and some of the calibration constants had to be adjusted based on these images. The velocity, density, and temperature values in the core are known from isentropic relations applied to the measured plenum and ambient conditions. The images were fit for ε, (x_0,y_0), r_R, and c_s, while u_k, r, and T were held fixed at the known isentropic values. The finesse profile determined from the calibration with particles was used in these fits. Light at the laser frequency and light scattered from particles were assumed negligible. Turbulent velocity fluctuations were assumed to be zero since the probe volume was well within the potential core and the uncertainty analysis showed that temperature estimates are not greatly affected by assuming zero turbulence when turbulence levels are small anyway. The broadband light and read noise were accounted for in the same way as in the reference fringe image processing described above. The mean ε, r_R-shift, and c_s values varied slightly from those determined in the particle-laden flow calibration. These calibration constants were used when particle scattering was negligible.

Using the calibration constants for particle-free flows, the image data taken in the potential core were fit for u_k, r, T, and (x_0,y_0) while assuming s_{uk}, A_p, and A_f were negligible. The difference between the measured u_k, r, and T values and the isentropic values as a function of velocity are shown in figure 7 for two different run days. The velocities fall within 5 m/s of their true (isentropic) values, densities are within 1.5 % of their true values, and temperatures are within 1% of their true values. The lowest velocity points were ignored for the error estimates since there is obviously something strange going on in the data as seen by the large error in the temperature at that velocity point. One hypothesis regarding the poor parameter estimates at low velocity is that when the fringe is pushed out near the radius of the image of the fiber face, some light spills over the edges of the image and is lost. The loss of this information imposes uncertainty in the measurements.

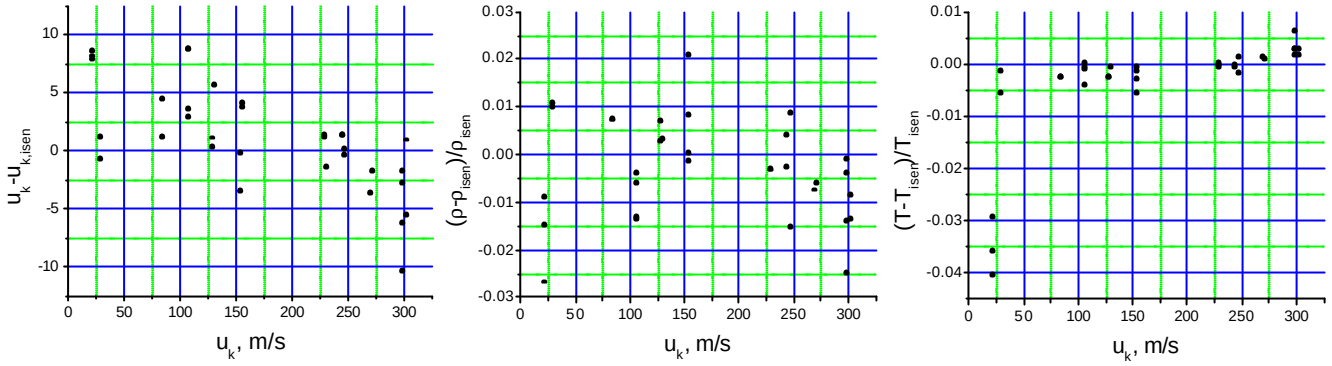

(a) (b) (c)

Fig. 7. Validation plots showing error in (a) velocity, (b) density, and (c) temperature obtained using the developed Rayleigh scattering technique for data taken in the jet potential core compared with isentropic values.

4.2 Converging nozzle, Mach 0.6 flow

Data were acquired at a series of radial and axial locations in a Mach 0.6 jet flow to determine flow profiles in terms of u_k, r, T, and s_{uk}. Using the appropriate calibration constants, the images were fit for u_k, r, T, s_{uk}, A_p, and (x_0,y_0). The amplitude of the particle scattering, A_p, was small in the jet core where there was no seeding, but increased to significant levels at radial locations (normalized by jet exit diameter, D) of r/D > 0.5, as shown in figure 8, and at axial stations of x/D > 6 due to entrainment of dust/smoke particles from the ambient air. The resulting velocity and turbulence estimates for radial scans at x/D = 4 and 6 are compared with hotwire measurements taken at the same locations in figures 9 and 10. The velocities compare well with the hotwire measurements with differences being on the order of ± 5 m/s. The turbulence estimates were within 5 m/s of the hotwire turbulence measurements for radial locations of r/D ≥ 0.5 where particles were present. The turbulence estimates were generally lower than the hotwire measurements outside the jet core. The turbulence estimates were higher than the expected values inside the jet core where particle density was extremely low. Particle scattering provided an additional feature in the spectrum with which to fit turbulence since the Mie scattering spectrum is broadened by the turbulent velocity fluctuations. As particle density is reduced, the ability to estimate turbulence declines. Density and temperature estimates corresponding to the radial scans at x/D = 4 and 6 for the Mach 0.6 jet are shown in figures 11 and 12 along with density and temperature predictions based on the C-B relations. Density estimates are within 4% and temperatures are within 2% of the C-B values. The uncertainty analysis showed that uncertainty in density and temperature increases with particle scattering. Fitting for particle scattering in the fringe images leads to higher uncertainties and a large degree of scatter in the density and temperature measurements; however, the measurements still give reasonable confidence in the temperature and density values obtained when fitting for turbulence.

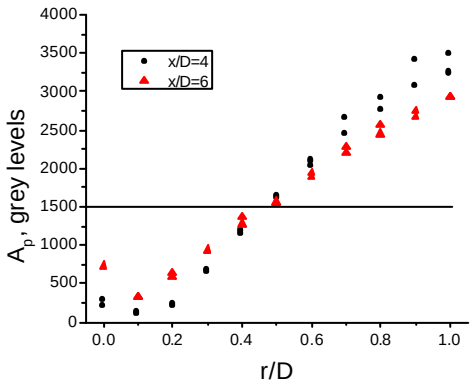

Fig. 8. Particle scattering amplitude for radial scans at x/D = 4 and 6 in Mach 0.6 jet.

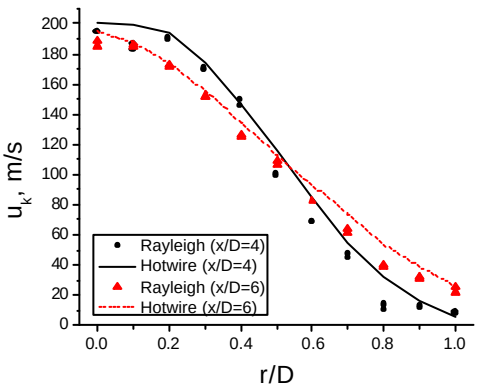

Fig. 9. Velocity profiles for radial scans at x/D = 4 and 6 in Mach 0.6 jet compared with hotwire measurements.

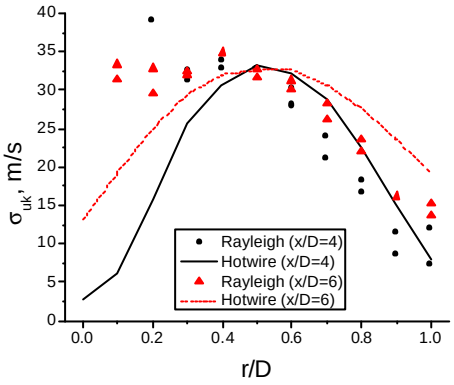

Fig. 10. Turbulence levels for radial scans at x/D = 4 and 6 in Mach 0.6 jet compared with hotwire measurements.

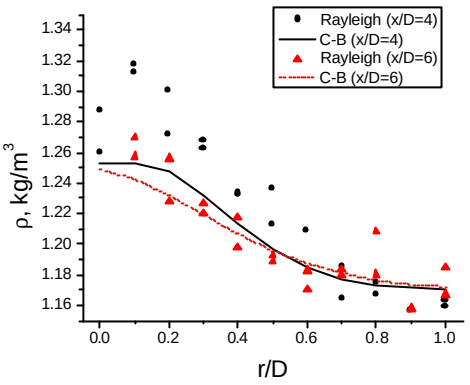

Fig. 11. Density profiles for radial scans at x/D = 4 and 6 in Mach 0.6 jet compared with Crocc-Busemann predictions.

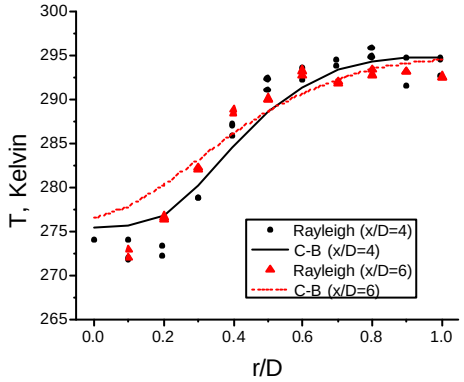

Fig. 12. Temperature profiles for radials scans at x/D = 4 and 6 in Mach 0.6 jet compared with Crocco-Busemann predictions.

Figures 13 and 14 show the velocity and turbulence measurements at axial locations along the centerline in the Mach 0.6 jet compared with hotwire measurements at the same locations. The velocity measurements compare well with the hotwire measurements at locations of x/D > 6 where particles are present. The turbulence estimates at these locations are generally higher than the hotwire measurements, but are still within 5 m/s as in the radial scans. In the potential core (x/D = 6) the parameter estimates have much higher uncertainty because there is a negligible amount of scattering from particles. The turbulence estimates blow up and the velocity measurements degrade when the least squares analysis tries to fit for information that is not available. This was proven to be the case by fitting the data in the potential core for u_k, r, T, and (x_0, y_0), while assuming A_p and s_{uk} were negligible. The improved velocity measurements are shown as open circles in figure 13.

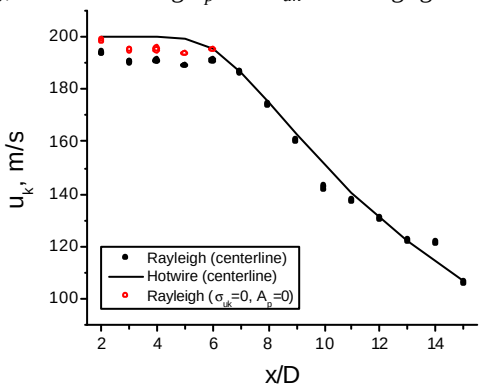

Fig. 13. Velocity profile for axial centerline scan in Mach 0.6 jet compared with hotwire measurements.

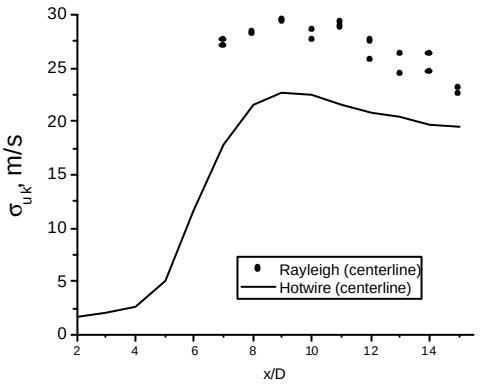

Fig. 14. Turbulence levels for axial centerline scan in Mach 0.6 jet compared with hotwire measurements.

4.3 Converging nozzle, Mach 0.95 flow

Surveys of a Mach 0.95 jet flow were performed and compared with available pitot tube data in the same flow. A centerline survey at axial stations from 2 to 20 diameters, and radial surveys at axial stations of 2, 4, 6, 8, 10, and 12 diameters were performed. There were particles present at radial stations outside of the shear layer and at axial stations far downstream of the nozzle exit. The velocity measurements for selected radial surveys far downstream where particles were fully entrained in the flow are shown in figure 15 along with the pitot tube velocity results for comparison. The velocities obtained from the Rayleigh image data are within 5 m/s of pitot tube velocity measurements. The turbulence estimates shown in figure 16 demonstrate that turbulence information was recovered over the entire radial range of the survey. Lau, et al. (1979) made

measurements of turbulence intensity in round nozzle flows using LDV. Turbulence estimates were extrapolated from their results and are shown in figure 16. The turbulence measurements from the Rayleigh scattering technique appear to be within 5 m/s of the expected values, except at locations close to the jet axis (r/D < 0.3) where the particle scattering amplitude was lower than the optimum value of 1500 grey levels. When A_p is lower than the optimum value the least squares analysis struggles to fit the Rayleigh and Mie peaks accurately since it becomes difficult to differentiate the two.

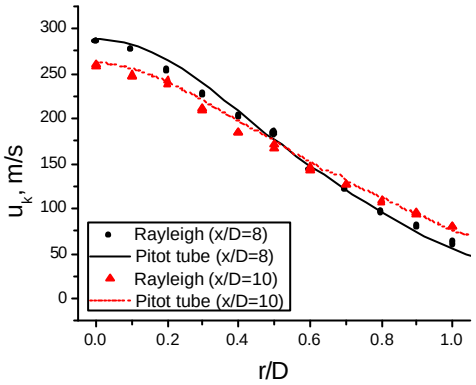

Fig. 15. Velocity profiles for radial scans at x/D = 8 and 10 in Mach 0.95 jet compared with pitot tube measurements.

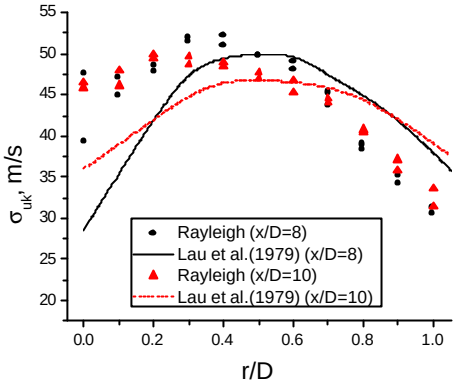

Fig. 16. Turbulence levels compared with published results for radial scans at x/D = 8 and 10 in Mach 0.95 jet.

4.4 Convergent-Divergent nozzle, Mach 1.4 flow

Axial and radial surveys of a Mach 1.4 jet flow were performed to demonstrate the viability of this technique in supersonic flows. Velocity results for the axial survey of the jet are shown in figure 17 along with pitot tube velocity measurements available for the same measurement stations. Rayleigh velocities are within 5 m/s of the pitot tube results except in the potential core (x/D < 7) where particle scattering is negligible. The values for velocity when A_p and s_{uk} are assumed negligible in the fitting of the data are shown as open circles, and demonstrate that the error is due to fitting for particle scattering when the amplitude is negligible. Turbulence results were obtained outside the jet core where particles were present and are shown in figure 18. Turbulence estimates extrapolated from Lau, et al. (1979) are also shown in the figure for comparison. As in the Mach 0.6 centerline scan, the turbulence estimates are about 5-8 m/s higher than the expected values, and the estimates blow up where particle scattering amplitude falls below the minimum acceptable level.

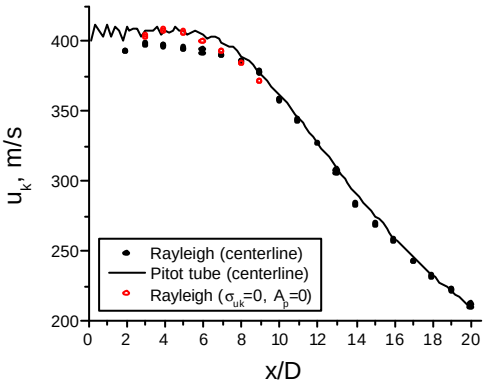

Fig. 17. Velocity profile for axial centerline scan in Mach 1.4 jet compared with pitot tube measurements.

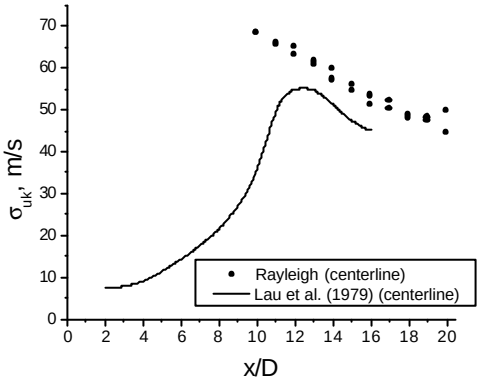

Fig. 18. Turbulence levels compared with published results for axial centerline scan in Mach 1.4 jet.

5. CONCLUDING REMARKS

A Rayleigh scattering technique to measure time-average velocity, density, temperature, and turbulence has been demonstrated in sparsely seeded gas flows. The velocity, density, and temperature measurements had accuracies of about 5 m/s, 1-4%, and 2%, respectively. Turbulence estimates were determined within 5 m/s in particle-laden flows as compared with hotwire measurements. Turbulence information could not be determined with any degree of accuracy in flows with low particle number density since there was not enough information available in the fringe pattern to extract turbulence.

The uncertainty in turbulence is high for small turbulence levels. A way to increase the accuracy of the turbulence measurements for small fluctuations is to use interferometer mirrors with higher finesse. Increasing finesse increases the resolution of the instrument, allowing small turbulence levels to be resolved. We plan to evaluate this measurement technique using interferometer mirrors with 99% reflectivity and finesse of about 300.
Parameter estimates at low velocities sometimes exhibited large uncertainties. The fringe diameter for low velocities is very large such that the outer edge of the fringe pattern is beyond the image of the fiber face. The loss of information in the fringe pattern may be the cause for these high uncertainties. To resolve this problem, a shorter focal length collimating lens may be used to increase the image of the fiber face at the detector plane. This allows imaging of the fringe pattern over a greater radial range.

Seeding flows is a tedious task, and as shown in this work, may degrade the accuracy of the density and temperature measurements. Therefore, it is desired to extend this measurement technique to work for unseeded flows. It may be possible to make turbulence measurements in unseeded flows in a near-forward scattering configuration. In this situation, the Rayleigh spectrum is in the Continuum regime and Brillioun peaks exist. The temperature is obtained from the separation of the Brillioun peaks, and the Rayleigh peak is no longer thermally broadened. This removes the correlation between turbulence and temperature in the spectral model. Future work is planned to make measurements in this scattering regime.

6. REFERENCES

Boley, C. D., Desai, R. C. & Tenti, G. (1972) "Kinetic models and Brillouin scattering in a molecular gas", *Can. J. Phys.* **50**, 2158-2173.

Bridges, J., Wernet, M. P., & Brown, C. (2003) "Control of jet noise through mixing enhancement", *NASA TM*-2003-212335.

Elliott, G. S. & Boguszki, M. (2001) "Filtered Rayleigh scattering: toward multiple property measurements", *AIAA*-2001-0301.

Flack, R. D. (1982) "Influence of turbulence scale and structure on individual realization laser velocimeter biases", *J. Phys. E: Sci. Instrum.* **15**, 1038-1044.

Garg, S. & Settles, G. S. (1998) "Measurements of a supersonic turbulent boundary layer by focusing schlieren deflectometry", *Exp. Fluids* **25**, 254-264.

Greytak, T. J. & Benedek, G. B. (1966) "Spectrum of light scattered from thermal fluctuations in gases", *Phys. Rev. Lett.* **17**, 179-182.

Hart, R. C., Balla, R. J. & Herring, G. C. (1999) "Nonresonant referenced laser-induced acoustics thermometry in air", *Appl. Optics* **38**, 577-584.

Heist, D. K. & Castro, I. P. (1996) "Point measurement of turbulence quantities in separated flows-a comparison of techniques", *Meas. Sci. Technol.* **7**, 1444-1450.

Lau, J. C., Morris, P. J. & Fisher, M. J. (1979) "Measurements in subsonic and supersonic free jets using a laser velocimeter", *J. Fluid Mech.* **93**, 1-27.

Lau, J. C., Whiffen, M. C., Fisher, M. J. & Smith, D. M. (1981) "A note on turbulence measurements with a laser velocimeter", *J. Fluid Mech.* **102**, 353-366.

Li, Y., Roberts, W. L. & Brown, M. S. (2002) "Investigation of gaseous acoustic damping rates by Transient Grating Spectroscopy", *AIAA J.* **40**, 1071-1077.

Mielke, A. F., Seasholtz, R. G., Elam, K. A. & Panda, J. (2004) "Time-average molecular Rayleigh scattering technique for measurement of velocity, density, temperature, and turbulence intensity in high speed nozzle flows", *AIAA*-2004-0706.

Panda, J. & Seasholtz, R. G. (1999) "Velocity and temperature measurement in supersonic free jets using spectrally resolved Rayleigh scattering", *AIAA*-99-0296.

Seasholtz, R. G. & Greer, L. C. (1998) "Rayleigh scattering diagnostic for measurement of temperature and velocity in harsh environments", *AIAA*-98-0206.

Seasholtz, R. G., Panda, J. & Elam, K. A. (2002) "Rayleigh scattering diagnostic for measurement of velocity and density fluctuation spectra", *AIAA*-2002-0827.

Tenti, G., Boley, C. D. & Desai, R. C. (1974) "On the kinetic model description of Rayleigh-Brillouin scattering from molecular gases", *Can. J. Phys.* **52**, 285-290.

Vaughan, J. M. (1989) *The Fabry Perot Interferometer, History, Theory, Practice, and Applications.* Adam Hilger.

Whalen, A. D. (1971) *Detection of Signals in Noise*. Academic Press.

White, F. M. (1973) *Viscous Fluid Flow*. McGraw-Hill.